

The perfectly matched layer for acoustic waves in absorptive media

Qing-Huo Liu and Jianping Tao

Citation: [The Journal of the Acoustical Society of America](#) **102**, 2072 (1997); doi: 10.1121/1.419657

View online: <http://dx.doi.org/10.1121/1.419657>

View Table of Contents: <http://asa.scitation.org/toc/jas/102/4>

Published by the [Acoustical Society of America](#)

Articles you may be interested in

[Convolutional perfectly matched layer for elastic second-order wave equation](#)

The Journal of the Acoustical Society of America **127**, (2010); 10.1121/1.3290999

[Application of the perfectly matched layer \(PML\) absorbing boundary condition to elastic wave propagation](#)

The Journal of the Acoustical Society of America **100**, (1998); 10.1121/1.417118

The perfectly matched layer for acoustic waves in absorptive media

Qing-Huo Liu and Jianping Tao

Klipsch School of Electrical and Computer Engineering, New Mexico State University, Las Cruces, New Mexico 88003

(Received 24 March 1997; revised 8 July 1997; accepted 9 July 1997)

The perfectly matched layer (PML) was first introduced by Berenger as a material absorbing boundary condition (ABC) for electromagnetic waves. It was first proven by Chew and Liu that a fictitious elastic PML half-space also exists in solids, which completely absorbs elastic waves, in spite of the coupling between compressional and shear waves. The PML absorbing boundary condition provides much higher absorption than other previous ABCs in finite-difference methods. In this work, a method is presented to extend the perfectly matched layer to simulating acoustic wave propagation in absorptive media. This nonphysical material is used at the computational edge of a finite-difference time-domain (FDTD) algorithm as an ABC to truncate unbounded media. Two aspects of the acoustic PML are distinct: (a) For a perfectly matched layer in an intrinsically absorptive medium, an additional term involving the time-integrated pressure field has to be introduced to account for the coupling between the loss from the PML and the normal absorptive loss; (b) In contrast to the full elastodynamic problem, the acoustic PML requires a splitting only on the pressure field, but not on the particle velocity field. The FDTD algorithm is validated by analytical solutions and other numerical results for two- and three-dimensional problems. Unlike the previous ABCs, the PML ABC effectively absorbs outgoing waves at the computational edge even when a dipping interface intersects the outer boundary. © 1997 Acoustical Society of America. [S0001-4966(97)05710-X]

PACS numbers: 43.30.Es, 43.30.Ky, 43.20.Bi, 43.30.Ma [SAC-B]

INTRODUCTION

Absorbing boundary conditions (ABCs) are important in numerical simulations of acoustic wave propagation in unbounded inhomogeneous media with partial-differential equation methods. These artificial boundary conditions are used in finite-difference or finite-element methods to eliminate the reflections from the outer boundary of the computational domain. Considerable efforts have been made in the development of various ABCs. Cerjan *et al.*¹ and Levander² use lossy materials near the computational edge to attenuate outgoing waves. However, since there is always a reflection between layers with different absorption coefficients, this ABC requires a substantial number of layers with a tapered profile of absorption in order not to produce noticeable reflections to the computational domain. Various other absorbing boundary conditions have been proposed to extrapolate the wave field at the boundary from the interior fields. Examples of such ABCs are those of Clayton and Engquist,³ Lindman,⁴ Randall,⁵ Liao,⁶ Higdon,⁷ and Peng and Toksöz.⁸ These ABCs, although successful in many applications, provide only limited absorption to waves within a specific range of incidence angles and frequencies. Furthermore, none of these ABCs can be applied to problems where a dipping interface intersects the outer boundary.

Recently, Berenger introduced a highly effective ABC based on the perfectly matched layer (PML) for electromagnetics.⁹ In the continuous limit, it is proven that a PML interface between a regular medium and such a fictitious perfectly matched medium completely absorbs incident waves from the regular medium, regardless of its incidence

angle and frequency.^{9,10} This new fictitious material has since been used extensively in the finite-difference time-domain (FDTD) simulations of electromagnetic waves. Chew and Liu^{11–13} first proved that such a perfectly matched layer also exists for elastic waves in spite of the coupling of transverse (S) and longitudinal (P) waves at an elastic interface. This new ABC has been implemented for two- and three-dimensional problems.^{11–13} Hastings *et al.* have independently implemented the PML ABC for two-dimensional elastic problems using potentials.¹⁴ Because of the use of potentials, however, the PML ABC in Ref. 14 unfortunately limits the applicability of the ABC to a homogeneous boundary. In contrast, the PML ABC developed by Chew and Liu^{11–13} is applicable to a boundary truncating any inhomogeneous medium.

Most previous effort on PML applications, however, has been concentrated on lossless media.^{9–14} For many applications, attenuation of acoustic waves due to the intrinsic loss is an important factor to characterize. In this work, the PML ABC is extended to scalar acoustic waves in absorptive media. The formulation is based on that in Refs. 11–13 and is analogous to that for electromagnetic waves in conductive media.¹⁵ For acoustic waves in absorptive media, the implementation of PML has to be modified to account for the coupling of loss from a PML and that from the regular absorption loss. One interesting aspect about the PML for acoustic waves is that, unlike the PML for elastic waves, the velocity field components need not be split. The PML ABC is implemented for two- and three-dimensional problems, and the numerical results are validated by analytical solu-

tions as well as FDTD results using Liao's absorbing boundary condition.⁶

I. FORMULATION

Consider a linear inhomogeneous, absorptive medium with space-dependent density $\rho(\mathbf{r})$, sound speed $c(\mathbf{r})$, and absorption coefficient $\gamma(\mathbf{r})$. The pressure field $p(\mathbf{r},t)$ and particle velocity $\mathbf{v}(\mathbf{r},t)$ field satisfy the basic Newton's law of motion and equation of continuity

$$\rho \frac{\partial \mathbf{v}(\mathbf{r},t)}{\partial t} = -\nabla p, \quad (1a)$$

$$\frac{\partial p}{\partial t} + \gamma(\mathbf{r})c^2(\mathbf{r})p(\mathbf{r},t) = -\rho(\mathbf{r})c^2(\mathbf{r})\nabla \cdot \mathbf{v}(\mathbf{r},t) + f_s(\mathbf{r},t), \quad (1b)$$

where $f_s(\mathbf{r},t)$ is the volume source density of pressure injection rate (Pa/s). In Eq. (1b), the absorption coefficient $\gamma(\mathbf{r})$ is used to characterize the absorptive loss in the medium. This absorption coefficient can be related to the attenuation coefficient $\alpha(\mathbf{r},\omega)$ by using the complex wave number $k(\mathbf{r},\omega) = \sqrt{\omega^2/c^2 + i\omega\gamma} = \omega/c'(\mathbf{r},\omega) + i\alpha(\mathbf{r},\omega)$, where $c'(\mathbf{r},\omega)$ is the dispersive wave velocity.

Before proceeding, we briefly discuss the implication of the acoustic medium dispersion properties on the causality of the wave field. For absorptive media, in general both $c(\omega)$ and $\gamma(\omega)$ in Eq. (1b) are frequency dependent in order for the wave field to remain causal. Mathematically, the dispersion relations for $c(\omega)$ and $\gamma(\omega)$ have to satisfy the following Kramers–Kronig relations:¹⁶

$$\frac{1}{c^2(\omega)} - \frac{1}{c^2(\infty)} = \frac{1}{\pi} \text{P.V.} \int_{-\infty}^{\infty} \frac{\gamma(\omega')/\omega'}{\omega' - \omega} d\omega', \quad (2a)$$

$$\frac{\gamma(\omega)}{\omega} = -\frac{1}{\pi} \text{P.V.} \int_{-\infty}^{\infty} \frac{1/c^2(\omega') - 1/c^2(\infty)}{\omega' - \omega} d\omega', \quad (2b)$$

where $c(\infty)$ is the value of $c(\omega)$ as the frequency approaches infinity, and P.V. stands for principal value integral. It can be concluded from Eqs. (2a) and (2b) that for an absorptive medium (i.e., $\gamma \neq 0$), $c(\omega)$ and $\gamma(\omega)$ have to vary as functions of frequency over the infinite range ($-\infty < \omega < \infty$). This, however, does not exclude the possibility of frequency-independent c and γ over a *finite* range of frequency, say $\omega_{\min} \leq \omega \leq \omega_{\max}$. Indeed, one can find many experimental measurements of such cases (for example, Ref. 17). For simplicity, therefore, in this work the acoustic medium is assumed dispersionless so that c and γ are independent of frequency over the bandwidth of interest. The following algorithm, however, can be readily modified to model dispersive media.

In the traditional finite-difference simulation of acoustic waves, Eqs. (1a) and (1b) are combined to obtain the following second-order partial-differential equation for the pressure field:

$$\rho \nabla \cdot \rho^{-1} \nabla p - \frac{1}{c^2} \frac{\partial^2 p}{\partial t^2} - \gamma \frac{\partial p}{\partial t} = -\frac{1}{c^2} \frac{\partial f_s}{\partial t}. \quad (3)$$

In the explicit second-order finite-difference schemes, solving Eq. (3) is more efficient than directly solving Eqs. (1a) and (1b). This is because only pressure fields at the two earlier time steps are needed in Eq. (3) to update the pressure at the next time step, while Eqs. (1a) and (1b) require four scalar variables (three velocity components and one pressure field) to update the wave field. With Eq. (3), various absorbing boundary conditions^{1–8} can be applied to truncate the unbounded medium in the finite-difference time-domain method.

A. Stretched coordinates for absorptive media

In this work, the perfectly matched layer (PML) will be used as an ABC. In order to introduce the PML for acoustic waves in absorptive media, the first-order equations in (1a) and (1b) will be modified using the stretched coordinates as proposed for electromagnetic waves and elastic waves.^{10–13} In the frequency domain, if the complex coordinate-stretching variable is chosen as

$$e_\eta = a_\eta + i \frac{\omega_\eta}{\omega} \quad (\eta = x, y, z), \quad (4)$$

the operator ∇_e expressed in terms of the complex coordinate-stretching variables is

$$\nabla_e = \sum_{\eta=x,y,z} \hat{\eta} \frac{1}{e_\eta} \frac{\partial}{\partial \eta}$$

Then by replacing ∇ with ∇_e , the first-order Eqs. (1a) and (1b) are modified in stretched coordinates as

$$-i\omega\rho\mathbf{v}(\mathbf{r},\omega) = -\sum_{\eta=x,y,z} \hat{\eta} \frac{1}{e_\eta} \frac{\partial p(\mathbf{r},\omega)}{\partial \eta}, \quad (5)$$

$$-i\omega p(\mathbf{r},\omega) + \gamma(\mathbf{r})c^2(\mathbf{r})p(\mathbf{r},\omega)$$

$$= -\rho(\mathbf{r})c^2(\mathbf{r}) \sum_{\eta=x,y,z} \frac{1}{e_\eta} \frac{\partial v_\eta(\mathbf{r},\omega)}{\partial \eta} + f_s(\mathbf{r},\omega), \quad (6)$$

where a time dependence of $e^{-i\omega t}$ is implied. In Eq. (4), for a PML region, the real part a_η is a scaling factor, and the imaginary part ω_η represents a loss in the PML. In a regular non-PML region, one has $a_\eta = 1$ and $\omega_\eta = 0$.

The addition of the real part a_η in (4) as an independent variable is to accelerate the attenuation to evanescent waves as well as waves in lossy media. This can be easily understood by considering plane waves e^{ikx} propagating in x direction with a complex wave number $k = k' + ik''$. Using $x = x'(a_x + i\omega_x/\omega)$, we have in the stretched coordinates,

$$e^{ikx} = e^{i(a_x k' - (\omega_x/\omega)k'')} e^{-(a_x k'' + (\omega_x/\omega)k')x'}, \quad (7)$$

which implies that the extra variable a_x provides an additional freedom to attenuate waves in lossy media further. The proof of zero reflections for a PML interface follows that in Refs. 11–13.

B. Splitting of equations in time domain

For time-domain simulations, the frequency-domain Eqs. (5) and (6) are inverse Fourier transformed into the time domain. By splitting the pressure field p and the source f_s into

$$p = \sum_{\eta=x,y,z} p^{(\eta)}, \quad f_s = \sum_{\eta=x,y,z} f_s^{(\eta)}, \quad (8)$$

and using (4), Eqs. (5) and (6) can be rewritten as

$$(-i\omega a_\eta + \omega_\eta) \rho v_\eta = -\frac{\partial p}{\partial \eta}, \quad (9)$$

$$\left[-i\omega a_\eta + (a_\eta \gamma c^2 + \omega_\eta) + \frac{i\omega_\eta \gamma c^2}{\omega} \right] p^{(\eta)} = -\rho c^2 \frac{\partial v_\eta}{\partial \eta} + \left(a_\eta + \frac{i\omega_\eta}{\omega} \right) f_s^{(\eta)}. \quad (10)$$

Inverse Fourier transforming the above two equations yields the time-domain equations

$$a_\eta \rho \frac{\partial v_\eta}{\partial t} + \omega_\eta \rho v_\eta = -\frac{\partial p}{\partial \eta}, \quad (11)$$

$$a_\eta \frac{\partial p^{(\eta)}}{\partial t} + (a_\eta \gamma c^2 + \omega_\eta) p^{(\eta)} + \omega_\eta \gamma c^2 \int_{-\infty}^t p^{(\eta)}(\mathbf{r}, t') dt' = -\rho c^2 \frac{\partial v_\eta}{\partial \eta} + a_\eta f_s^{(\eta)}(\mathbf{r}, t) + \omega_\eta \int_{-\infty}^t f_s^{(\eta)}(\mathbf{r}, t') dt'. \quad (12)$$

From the above derivation, it is worthwhile to note the following important difference between an acoustic PML and an elastic PML: In the acoustic PML, there is no need to split the particle velocity \mathbf{v} into $\mathbf{v}^{(\eta)}$ as in the elastic PML. This is simply because the second-rank stress tensor in the elastic case collapses into a zero-rank tensor (i.e., a scalar pressure field) in the acoustic case. Equations (11) and (12) consist of a total of six scalar equations. In addition, the third term in (12) requires three additional variables for each cell. Therefore, the memory requirement in the PML region is 4.5 times that required by a regular acoustic medium with the same dimension. This extra memory requirement in the boundary PML region is offset by the effectiveness of PML in absorbing the outgoing waves. Note also that with the introduction of PML, there is an additional term involving the time-integrated pressure field in Eq. (12). This term represents the coupling of the loss in PML with the regular absorption loss. The split equations (11) and (12) can then be solved by the following FDTD method.

II. FINITE-DIFFERENCE IMPLEMENTATION

In view of the computer memory requirement in the PML region, the computational domain may be partitioned into a regular interior region and the boundary PML region, as shown in Fig. 1, to save memory. In the interior region, only the pressure field is used in a centered grid to discretize the second-order equation (3). In the boundary region consisting of several PMLs, both the pressure and the particle velocity fields are used in a staggered grid, as shown in Fig.

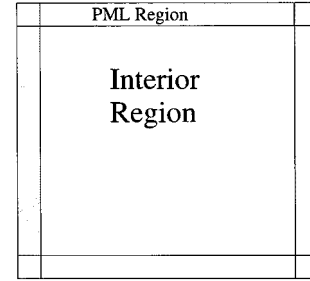


FIG. 1. Computational domain with an interior region and a PML boundary region. The second-order partial differential equation for p may be used for the interior region, while the first-order split equations are used for the PML region.

2 for a unit cell, to discretize the first-order equations (11) and (12). Alternatively, on a parallel computer, in terms of data structure it may be more advantageous to use the first-order equations (11) and (12) throughout the whole computational domain, and simply let $a_\eta = 1$, $\omega_\eta = 0$ for the interior region.

The staggered grid in Fig. 2 is a reduced one from the full elastic staggered grid.¹⁸ In this staggered grid, the pressure field p is located at the cell center, while the velocity field components are located at the cell's face centers. The unbounded medium is truncated into a finite computational domain with a total of $N_x \times N_y \times N_z$ cells. If the finite-difference cell size is Δx , Δy , and Δz in x , y , and z directions, respectively, the pressure field and velocity field components are discretized as

$$p^{(\eta)}(j_x, j_y, j_z, n) \equiv p^{(\eta)}[(j_x + \frac{1}{2})\Delta x, (j_y + \frac{1}{2})\Delta y, (j_z + \frac{1}{2})\Delta z, n\Delta t], \quad (13a)$$

$$v_x(j'_x, j_y, j_z, n) \equiv v_x[j'_x \Delta x, (j_y + \frac{1}{2})\Delta y, (j_z + \frac{1}{2})\Delta z, (n + \frac{1}{2})\Delta t], \quad (13b)$$

$$v_y(j_x, j'_y, j_z, n) \equiv v_y[(j_x + \frac{1}{2})\Delta x, j'_y \Delta y, (j_z + \frac{1}{2})\Delta z, (n + \frac{1}{2})\Delta t], \quad (13c)$$

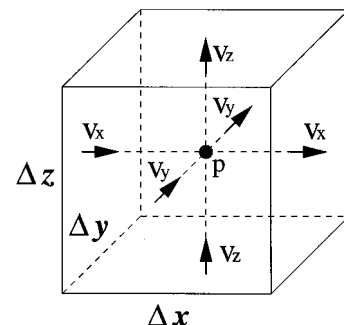


FIG. 2. The relative locations of field components in a unit cell of the staggered grid for the PML region.

$$v_z(j_x, j_y, j_z', n) = v_z[(j_x + \frac{1}{2})\Delta x, (j_y + \frac{1}{2})\Delta y, j_z' \Delta z, (n + \frac{1}{2})\Delta t], \quad (13d)$$

where n is an integer, $j_\eta = 0, \dots, N_\eta - 1$, and $j'_\eta = 0, \dots, N_\eta$. The central differencing is used for both the spatial and temporal derivatives. Furthermore, the second and third terms on the left-hand side of Eq. (12) require the averaging of their values at $t=n\Delta t$ and $t=(n+1)\Delta t$, since p is not evaluated at $t=(n+1/2)\Delta t$. This averaging has the same second-order accuracy as the central differencing used for the first term on the left-hand side of (12), and therefore does not degrade the overall accuracy in the discretization.

With this discretization, Eq. (11) becomes a time-stepping equation. For example, the time-stepping equation for v_x is

$$\begin{aligned} v_x(j'_x, j_y, j_z, n) &= f_{1x}v_x(j'_x, j_y, j_z, n-1) \\ &\quad + f_{2x}[p(j'_x, j_y, j_z, n) \\ &\quad - p(j'_x - 1, j_y, j_z, n)], \end{aligned} \quad (14)$$

where

$$f_{1\eta} = \frac{a_\eta/\Delta t - \omega_\eta/2}{a_\eta/\Delta t + \omega_\eta/2}, \quad f_{2\eta} = -\frac{1}{(a_\eta/\Delta t + \omega_\eta/2)\rho\Delta\eta}. \quad (15)$$

For the pressure field $p^{(x)}$, Eq. (12) becomes

$$\begin{aligned} p^{(x)}(j_x, j_y, j_z, n+1) &= f_{3x}p^{(x)}(j_x, j_y, j_z, n) + f_{4x}p_I^{(x)}(j_x, j_y, j_z, n) \\ &\quad + f_{5x}[v_x(j_x + 1, j_y, j_z, n) - v_x(j_x, j_y, j_z, n)] \\ &\quad + f_{6x}f_s(j_x, j_y, j_z, n + \frac{1}{2}), \end{aligned} \quad (16)$$

where

$$f_{3\eta} = \frac{a_\eta/\Delta t - (a_\eta\gamma c^2 + \omega_\eta)/2}{D_{\eta v}}, \quad f_{4\eta} = -\frac{\omega_\eta\gamma c^2\Delta t}{D_{\eta v}}, \quad (17)$$

$$f_{5\eta} = -\frac{\rho c^2}{D_{\eta v}}, \quad f_{6\eta} = \frac{1}{D_{\eta v}}, \quad (18)$$

$$\begin{aligned} p_I^{(\eta)}(j_x, j_y, j_z, n) &= \frac{1}{2} p^{(\eta)}(j_x, j_y, j_z, 0) \\ &\quad + \sum_{l=1}^n p^{(\eta)}(j_x, j_y, j_z, l), \end{aligned} \quad (19)$$

and $D_{\eta v} = a_\eta/\Delta t + (a_\eta\gamma c^2 + \omega_\eta)/2 + \omega_\eta\gamma c^2\Delta t/2$. Similar expressions can be derived for the other field components. In Eq. (16), the source f_s is assumed to be located at a regular non-PML region. Otherwise, a time-integrated source term should be added as in the last term on the right-hand side of Eq. (12). It should be noted that the material parameters in Eqs. (15), (17), and (18) must be properly averaged in order to arrive at a higher accuracy.¹⁸

Equations (14) and (16) constitute a leapfrog system for v_η and $p^{(\eta)}$ ($\eta = x, y, z$). Given a particular source excitation $f_s(\mathbf{r}, t)$, this time-stepping system provides the wave field solutions for the entire grid. The absorption of outgoing

waves is achieved by the PML region, which consists of several (typically 10) cells of PML materials with a quadratically or linearly tapered profile to increase the attenuation toward the outer boundary. For example, near the boundary $x=0$, ω_x for the $M=10$ cells of the PML region is chosen as

$$\omega_x(j_x) = \frac{(M-1/2-j_x)^p}{(M-1/2)^p} \omega_{x,\max} \quad (j_x = 0, \dots, M-1), \quad (20)$$

where $\omega_{x,\max}$ is the value at the center of the first cell. At the outer boundary, the normal component of the velocity is forced to zero. This rigid boundary condition does not give rise to reflections into the interior region because of the PML region. It is found that the quadratic profile ($p=2$) gives a better absorption than the linear profile ($p=1$).

III. NUMERICAL RESULTS

We have implemented the FDTD algorithm with the perfectly matched layers as the absorbing boundary condition for two and three dimensions. Unlike the continuous case, some reflection will occur at the discretized PML interface. This reflection is proportional to the contrast in the coordinate-stretching variables. Therefore, to minimize the reflection from the PML layers, we choose a linear profile for the PML coordinate-stretching variables. Typically we use 10 cells of perfectly matched layers at the computational edge.

In the following examples, a monopole source is used to excite the acoustic wave field. The time function $f_s(t)$ of the source is the first derivative of the Blackman–Harris window function.^{15,18} The central frequency of this time function is chosen as $f_c = 2$ kHz.

A. A 2-D homogeneous absorptive medium

The first simple testing case for the FDTD algorithm is a homogeneous medium with $\rho = 1200$ kg/m³, $c = 1500$ m/s, $\gamma = 2 \times 10^{-3}$ s/m² in two dimensions. The monopole line source is located at $(x, y) = (1.1, 1.1)$ m, and the pressure field p is calculated at 18 locations $x_i = 1.0 + (i-1) \times 0.05$, $y_i = 1.15$ m ($i = 1, \dots, 18$). The 2-D FDTD program is used to model a problem with $N_x \times N_y = 88 \times 88$ cells with 12 perfectly matched layers on each side of the computational domain. The cell size is $\Delta x = \Delta y = 0.025$ m. To verify the numerical results, an analytical solution is obtained by inverse Fourier transforming the following frequency-domain solution

$$p(\mathbf{r}, \omega) = \frac{\omega}{4c^2} H_0^{(1)}(kr) F_s(\omega), \quad (21)$$

where $F_s(\omega)$ is the Fourier transform of $f_s(t)$ and $k = \sqrt{\omega^2/c^2 + i\omega\gamma}$.

The 2-D FDTD results are compared with the analytical solutions in Fig. 3(a) for the array. Note that the results are normalized with respect to the peak value of the field at the third receiver (nearest receiver to the source). Figure 3(b) shows more clearly the comparison with analytical solution

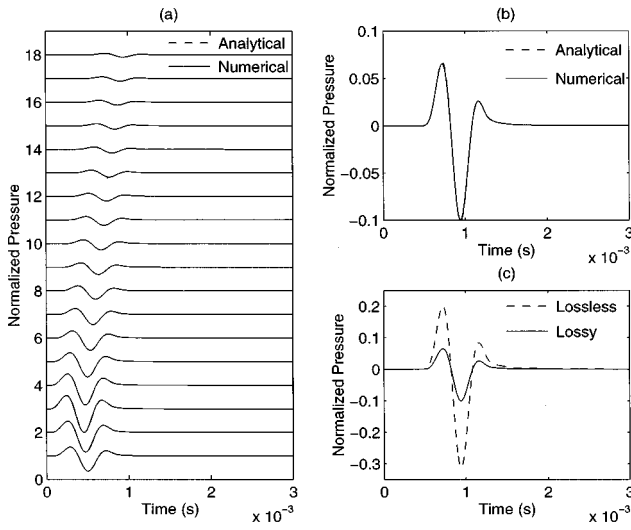


FIG. 3. FDTD results and analytical solutions for a monopole line source in a 2-D homogeneous medium. (a) Pressure waveforms at 18 receiver locations for a lossy medium ($\gamma=2\times 10^{-3}$ s/m 2). (b) The results of (a) at the 18th receiver. (c) FDTD results for the lossy ($\gamma=2\times 10^{-3}$ s/m 2) and lossless media at the 18th receiver location.

for the 18th receiver. Excellent agreement is observed between the numerical and analytical results. In Fig. 3(c), the pressure field at the 18th receiver is compared with that for the case where the absorption loss is zero (also obtained by the FDTD program). It shows that the absorption introduces an attenuation of about 9.84 dB to the peak value of the wave field at this location.

From the above results, it is seen that the PML ABC provides an effective attenuation to the outgoing waves since no reflections are observable from the wave forms in Fig. 3. In order to characterize the performance of the PML ABC quantitatively, snapshots are shown in Fig. 4 for the case without absorption loss in the interior medium. With a time step of $\Delta t=5\ \mu\text{s}$, the direct wave from the source has already reached outside the computational domain after the time step $n=300$ shown in Fig. 4(e). Since the relative maximum amplitudes of Fig. 4(a)–(i) with respect to (b) is $-4.56, 0, -8.06, -10.13, -25.58, -43.97, -52.95, -55.59$, and -63.40 dB, respectively, the amplitude of the reflected wave is estimated to be in the order of -50 dB with respect to Fig. 4(b). The maximum field amplitude (normalized with respect to $n=120$) as a function of the time steps is shown in Fig. 5(a). The horizontal slice of the pressure field (absolute value) through the source location is shown for these time steps in Fig. 5(b)–(d). As noted from these slices, the symmetry of the wave field is exactly preserved in the finite-difference program.

B. An absorptive cylinder in an absorptive background medium

This tests the two-dimensional program with an absorptive circular cylinder in an absorptive background medium. The monopole line source is located at the center of the cylinder at $(x,y)=(1.1,1.1)$ m as for Fig. 3. The receiver locations are also the same. The cylinder (radius $a=0.4$ m) with $\rho_1=1200\ \text{kg/m}^3$, $c_1=1500\ \text{m/s}$, $\gamma_1=2\times 10^{-3}\ \text{s/m}^2$ is

surrounded by a background medium with $\rho_2=1000\ \text{kg/m}^3$, $c_2=1000\ \text{m/s}$, $\gamma_2=0.05\ \text{s/m}^2$. The discretization is the same as for the last case. The analytical solution for the pressure field is given by

$$p(\mathbf{r},\omega)=\begin{cases} \frac{\omega}{4c_1^2}[H_0^{(1)}(k_1r)+RJ_0(k_1r)]F_s(\omega), & r\leq a \\ \frac{\omega}{4c_1^2}TH_0^{(1)}(k_2r)F_s(\omega), & r\geq a, \end{cases} \quad (22)$$

where (ρ_1, c_1, γ_1) and (ρ_2, c_2, γ_2) are, respectively, the medium parameters inside and outside the cylinder, and $k_j=\sqrt{\omega^2/c_j^2+i\omega\gamma_j}$ for $j=1,2$. The reflection and transmission coefficients are given by

$$R=-\frac{k_2\rho_1H_0^{(1)}(k_1a)H_0^{(1)\prime}(k_2a)-k_1\rho_2H_0^{(1)\prime}(k_1a)H_0^{(1)}(k_2a)}{D_c(\omega)}, \quad (23)$$

$$T=-\frac{2i\rho_2/\pi a}{D_c(\omega)}, \quad (24)$$

where

$$D_c(\omega)=k_2\rho_1J_0(k_1a)H_0^{(1)\prime}(k_2a) - k_1\rho_2J_0'(k_1a)H_0^{(1)}(k_2a) \quad (25)$$

is the denominator of (23) and (24).

With the configuration of the measurement system, the 1st through 11th receivers measure the incident and reflected waves since they are located within the cylinder, while the 12th through 18th receivers measure the transmitted wave since they are outside the cylinder. The numerical results are compared with analytical solutions for the first 11 receivers in Fig. 6(a), and for the last 7 receivers in Fig. 6(b). Note that the field is normalized with respect to the field at the third receiver, the nearest one from the source. In order to show the transmitted wave clearly, Fig. 6(b) is magnified by a factor of 20. Excellent agreement is observed for fields both inside and outside the cylinder.

In order to see the effect of the absorption loss to the wave field, the above medium is also modeled without loss (i.e., $\gamma_1=\gamma_2=0$). The numerical and analytical results for the lossless medium are shown in Fig. 7(a) and (b) for the field inside and outside the cylinder. The field is again normalized with respect to the field at the third receiver (the normalization factor is about 1.106 times that in Fig. 6). Note that a much larger transmitted field is observed since Fig. 7(b) is now only magnified by a factor of 3.

C. A 3-D homogeneous absorptive medium

Similarly, the 3-D FDTD program was validated first for a monopole point source in a three-dimensional homogeneous medium. The example under investigation is exactly the same as for Fig. 3 except that this is for a monopole point source at $(x,y,z)=(1.1,1.1,1.1)$ m, and the pressure field p is calculated at 18 locations $x_i=1.0+(i-1)\times 0.05, y_i$

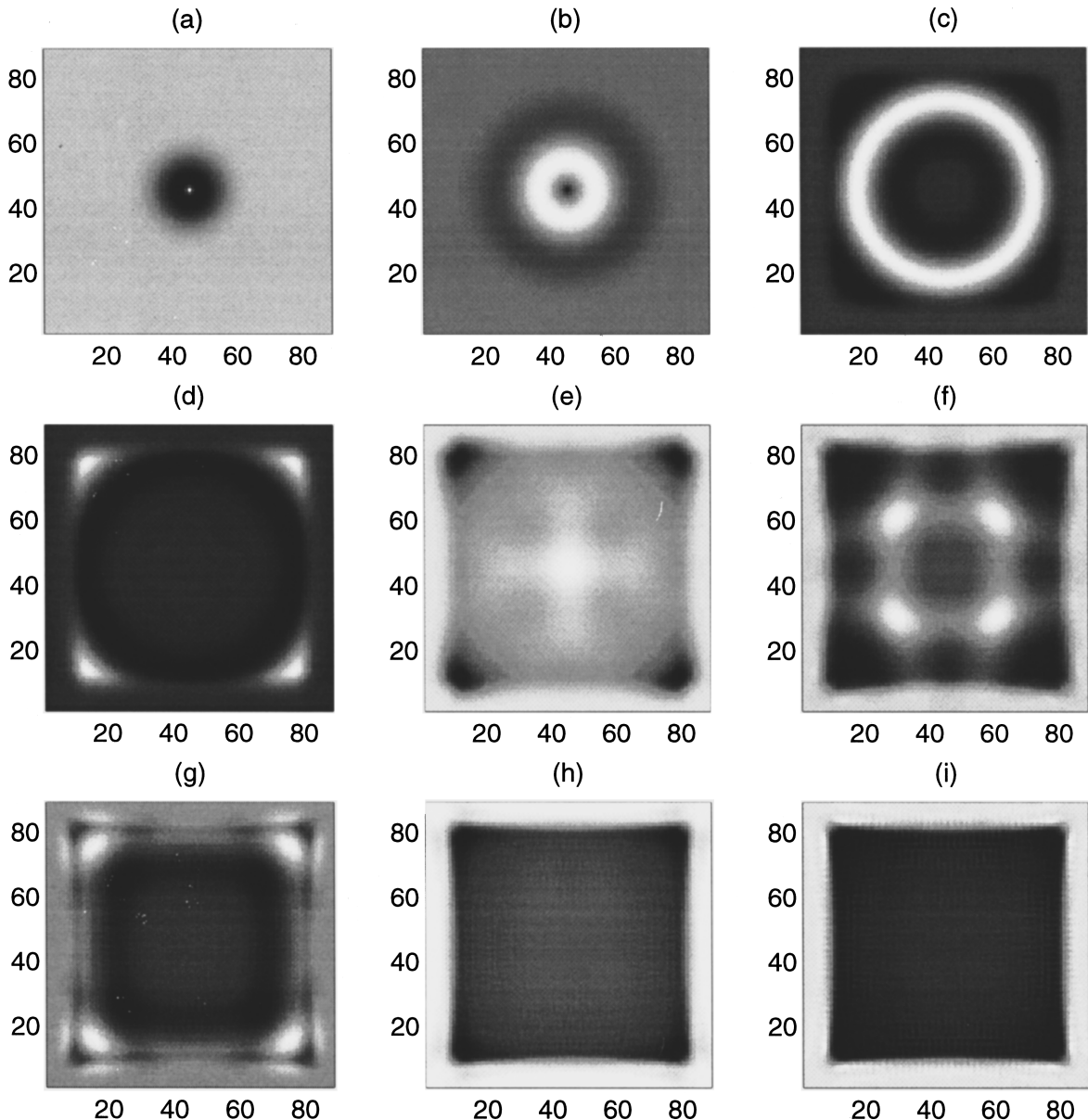


FIG. 4. From (a) to (i), the FDTD snapshots for the lossless medium in Fig. 3(c) at time steps $n=60, 120, 180, 240, 300, 360, 420, 480$, and 540 . The time-step increment is $\Delta t=5 \mu\text{s}$. The relative maximum amplitudes of (a) to (i) with respect to (b) is $-4.56, 0, -8.06, -10.13, -25.58, -43.97, -55.59$, and -63.40 dB , respectively.

$= 1.15$, $z_i = 1.1 \text{ m}$ ($i = 1, \dots, 18$). The 3-D FDTD program is used to model a problem with $N_x \times N_y \times N_z = 88 \times 88 \times 88$ cells with 12 perfectly matched layers on each side of the computational domain. The discretization is $\Delta x = \Delta y = \Delta z = 0.025 \text{ m}$ and $\Delta t = 5 \mu\text{s}$. The analytical solution in the frequency domain is

$$p(\mathbf{r}, \omega) = -\frac{i\omega}{4\pi c^2 r} e^{ikr} F_s(\omega). \quad (26)$$

The comparison between the 3-D FDTD results and analytical solutions is shown in Fig. 8 for the last 11 receivers. As for the 2-D FDTD results, the 3-D numerical results agree well with the analytical solutions. As expected, in contrast to the 2-D case in Fig. 3, the waveforms in Fig. 8 have exactly the same symmetric shape as the derivative of the source time function $f'_s(t)$. In the 2-D case, the waveforms become

skewed because of the insonification of the infinitely long line source.

D. An absorptive sphere in an absorptive background medium

Another special case where analytical solutions are available is a monopole point source in an absorptive sphere. The monopole source is located at the center of the sphere (radius $a = 0.4 \text{ m}$) with $\rho_1 = 1200 \text{ kg/m}^3$, $c_1 = 1500 \text{ m/s}$, $\gamma_1 = 2 \times 10^{-3} \text{ s/m}^2$ surrounded by a background medium with $\rho_2 = 1000 \text{ kg/m}^3$, $c_2 = 1000 \text{ m/s}$, $\gamma_2 = 0.05 \text{ s/m}^2$. The locations of the source and receivers, as well as the discretization, are the same as for Fig. 8. The analytical solution for the pressure field is given by

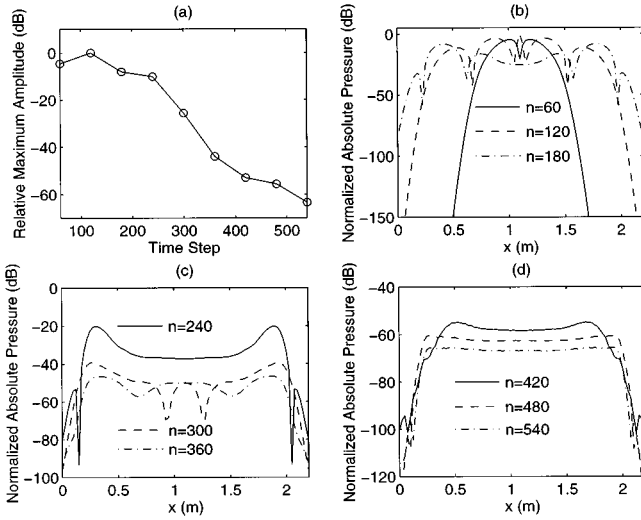


FIG. 5. (a) Corresponding to Fig. 4, the maximum field amplitude as a function of time steps. Horizontal slice of the field (absolute value) through the source location for (b) $n=60,120,180$; (c) $n=240,300,360$; (d) $n=420,480,540$. The field is normalized with respect to the maximum of the field at $n=120$.

$$p(\mathbf{r}, \omega) = \begin{cases} \frac{\omega k_1}{4\pi c_1^2} [h_0^{(1)}(k_1 r) + R j_0(k_1 r)] F_s(\omega), & r \leq a, \\ \frac{\omega k_2}{4\pi c_1^2} T h_0^{(1)}(k_2 r) F_s(\omega), & r \geq a, \end{cases} \quad (27)$$

where (ρ_1, c_1, γ_1) and (ρ_2, c_2, γ_2) are, respectively, the medium parameters inside and outside the sphere, and $k_j = \sqrt{\omega^2/c_j^2 + i\omega\gamma_j}$ for $j=1,2$. The reflection and transmission coefficients are given by

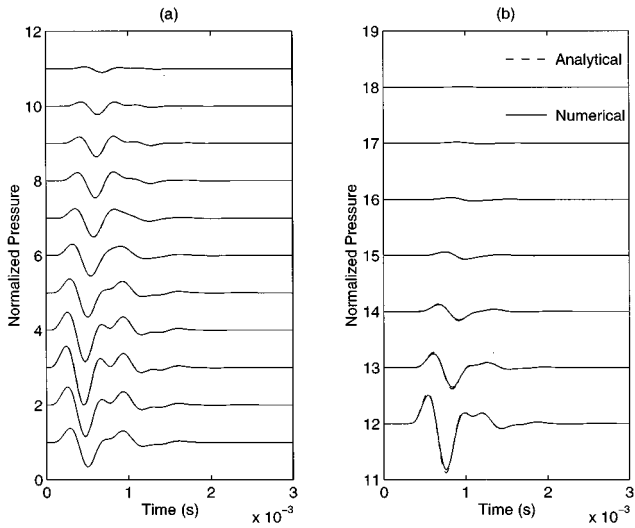


FIG. 6. A monopole line source at the center of an absorptive circular cylinder (radius 0.4 m) in an absorptive medium. The normalized pressure field (with respect to the third receiver) (a) inside the cylinder for the first through 11th receivers, and (b) outside the cylinder for the 12th through 18th receivers. The results for (b) are magnified by a factor of 20.

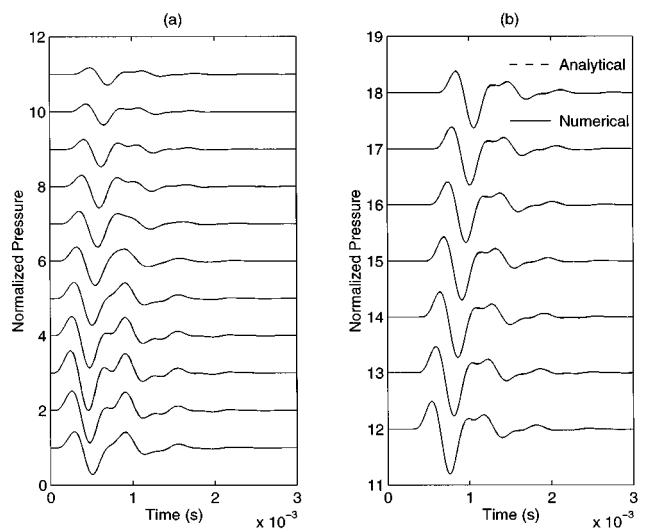


FIG. 7. Same as Fig. 6 except for a lossless cylinder in a lossless background medium (i.e., $\gamma_1 = \gamma_2 = 0$). The results for (b) are magnified by a factor of 3.

$$R = -\frac{k_2 \rho_1 h_0^{(1)}(k_1 a) h_0^{(1)'}(k_2 a) - k_1 \rho_2 h_0^{(1)'}(k_1 a) h_0^{(1)}(k_2 a)}{D_s(\omega)} \quad (28)$$

$$T = \frac{i \rho_2 / k_2 a^2}{D_s(\omega)}, \quad (29)$$

where

$$D_s(\omega) = k_2 \rho_1 j_0(k_1 a) h_0^{(1)'}(k_2 a) - k_1 \rho_2 j_0'(k_1 a) h_0^{(1)}(k_2 a). \quad (30)$$

Figure 9(a) shows the excellent agreement between the numerical and analytical results both inside and outside the

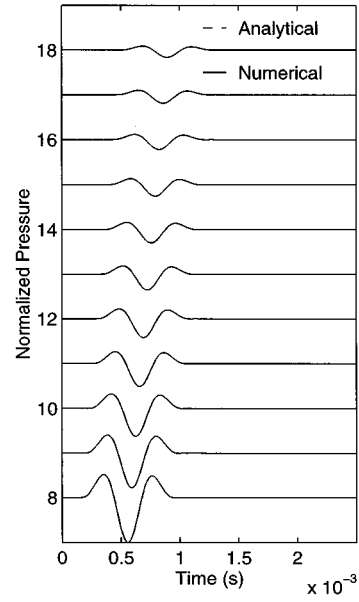


FIG. 8. A monopole point source in an homogeneous absorptive medium with $\rho = 1200 \text{ kg/m}^3$, $c = 1500 \text{ m/s}$, $\gamma = 2 \times 10^{-3} \text{ s/m}^2$. The source is located at $(x, y, z) = (1.1, 1.1, 1.1) \text{ m}$, and the receivers are at $x_i = 1.0 + (i-1) \times 0.05$, $y_i = 1.15$, $z_i = 1.1 \text{ m}$ ($i = 8, \dots, 18$).

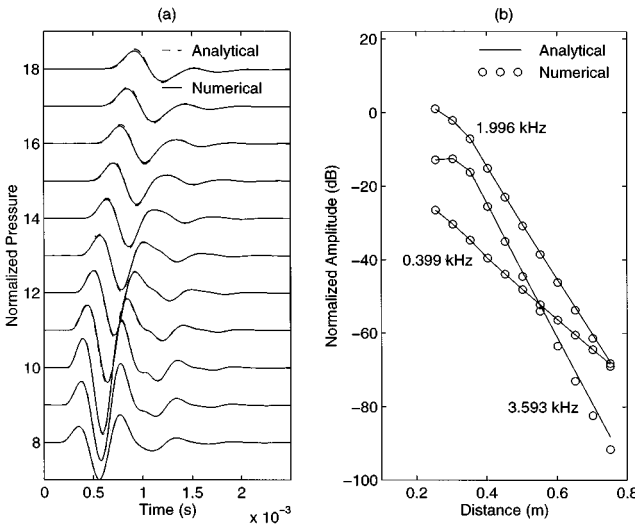


FIG. 9. A monopole point source at the center of an absorptive sphere (radius 0.4 m, $\rho_1=1200 \text{ kg/m}^3$, $c_1=1500 \text{ m/s}$, $\gamma_1=2 \times 10^{-3} \text{ s/m}^2$) in a homogeneous absorptive medium with $\rho_2=1000 \text{ kg/m}^3$, $c_2=1000 \text{ m/s}$, $\gamma_2=0.05 \text{ s/m}^2$. The locations of the source and receivers are the same as in Fig. 8. (a) Transient waveforms, (b) spectral amplitude as a function of receiver distance for $f=0.399$, 1.996 , and 3.593 kHz.

sphere for the last 11 receivers. To demonstrate that the field calculated by the FDTD method indeed has a correct attenuation, we perform a Fourier transform on the transient waveforms in Fig. 9(a). The spectral amplitude of the pressure field is plotted for three frequencies (low end, center, and high end of the source frequency band) in Fig. 9(b) as a function of the receiver distance from the source, and normalized with respect to the amplitude near the central frequency (1.996 kHz). Overall, the numerical results agree well with analytical solutions. At the high end of the frequency band (3.593 kHz), the error becomes larger. This is typical of FDTD methods, since with a finite cell size ($\Delta x, \Delta y, \Delta z$), both the geometry representation and the spatial derivatives give rise to a larger error at high frequency. The error can be further reduced by refining the cell size.

E. Comparison with Liao's ABC

One important application of this algorithm is in simulations of acoustic wave propagation in underwater environments. Typically the ocean surface and sea floor have to be incorporated in the model. Unfortunately, most existing absorbing boundary conditions cannot be used for such applications if these interfaces have a dip. Under the special case where the interfaces intersect with the computational boundary perpendicularly, Liao's ABC can be used to simulate the wave propagation in FDTD methods. In this example, we compare the FDTD results using PML ABC with those of Liao's ABC^{6,18} for an acoustic measurement in a flat ocean. The three (from top to bottom $j=1,2,3$) layers have the following properties: $\rho_j=1000, 1200, 2200 \text{ kg/m}^3$; $c_j=1000, 1500, 2500 \text{ m/s}$. These layers extend to the full range in the y direction. Two rectangular cylinders ($\rho=2000 \text{ kg/m}^3$, $c=2000 \text{ m/s}$) are in the second layer and extend from $y=0.7$ to $y=0.9 \text{ m}$. The medium is lossless. The $x-z$ cross section at $y=0.8 \text{ m}$ is shown in Fig. 10(a). A monopole

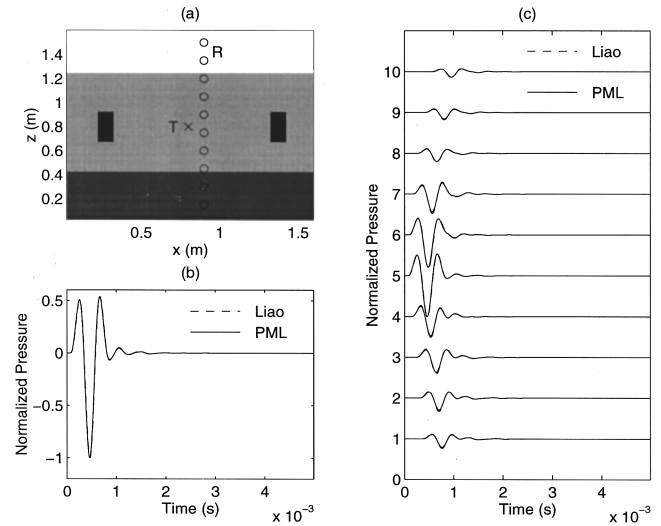


FIG. 10. Comparison of PML ABC and Liao's ABC for acoustic wave propagation in a three-layer medium with rectangular blocks. (a) Configuration. Pressure field at the fifth receiver (b) and at the array receivers (c).

source is located at $(x,y,z)=(0.8,0.8,0.8) \text{ m}$, and an array of 10 receivers is located vertically at $x_j=0.9$, $y_j=0.8$, and $z_j=0.15j \text{ m}$ ($j=1,\dots,10$).

We compare the 3-D FDTD results using PML ABC with those using Liao's ABC, as shown in Fig. 10(b) for the fifth receiver. Figure 10(c) shows the total pressure field at the receiver array. It is seen that the agreement is excellent. In contrast to the PML ABC, the Liao's ABC, however, requires a double precision in order to be stable.

F. A dipping interface in underwater acoustic measurements

Dipping interfaces are often encountered and are therefore very important for underwater acoustic measurements. Unfortunately, previous absorbing boundary conditions cannot model these dipping interfaces since all of them require at least homogeneity in the direction perpendicular to the truncating boundary. The PML absorbing boundary condition, therefore, offers an unparalleled advantage over other ABC's for these problems.

We illustrate such applications of PML's for a dipping layer shown in Fig. 11(a). The configuration for the three layers is the same as in Fig. 10(a), except that the bottom layer is dipping. In addition, the two rectangular cylinders are replaced by two spheres (radii 0.2 m) located at the same centers. The monopole point source is located at the center of the left sphere, while an array of 31 receivers is located at the top interface. For this problem with a dipping interface, the FDTD algorithm with PML ABC is stable, whereas with Liao's ABC, the algorithm becomes unstable as soon as the waves propagate to the boundary. Figure 11(b) shows the pressure field measured at the 16th receiver, while Fig. 11(c) shows the array waveforms.

G. A large two-dimensional problem

Finally, a large two-dimensional problem is investigated for underwater acoustics as an example of applications. The

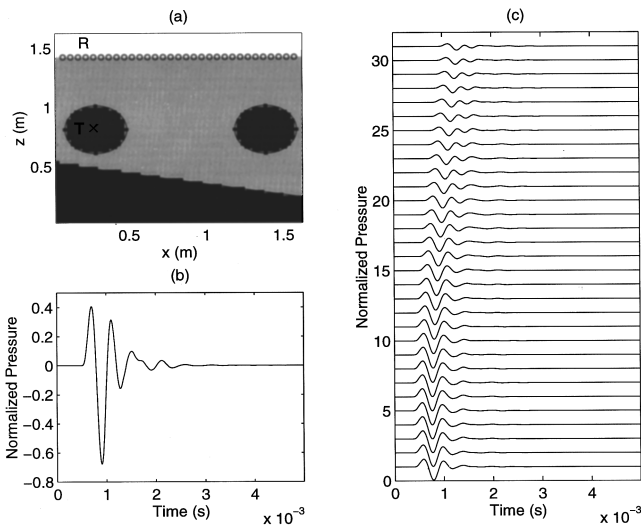


FIG. 11. Simulation of acoustic wave propagation using a 3-D FDTD program with PML ABC for a three-layer medium with two spheres. (a) Configuration. Pressure field at the 16th receiver (b) and at the array receivers (c).

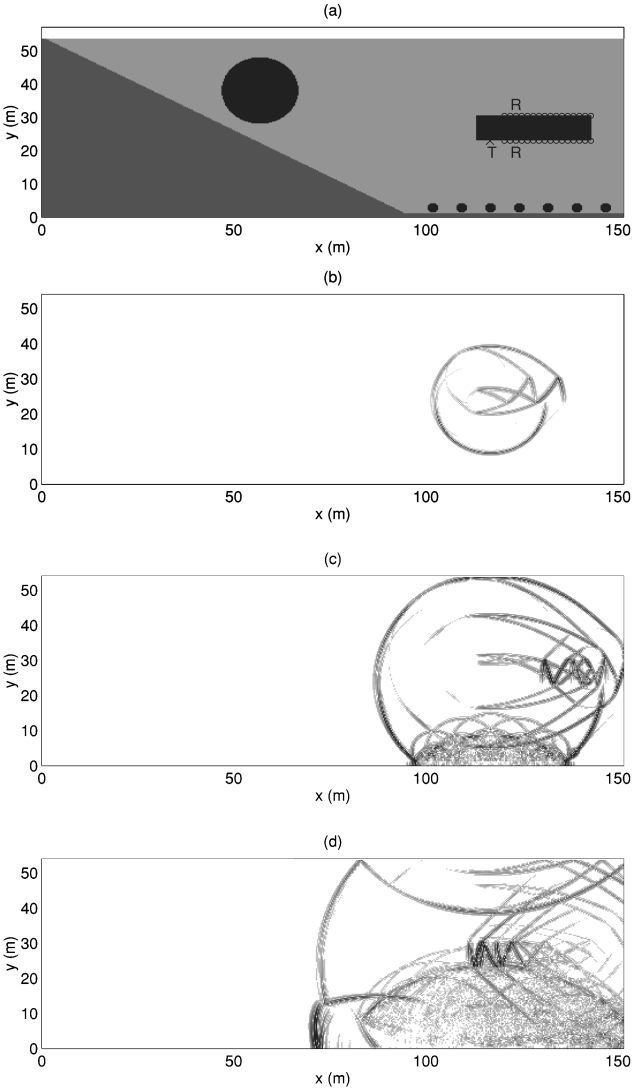
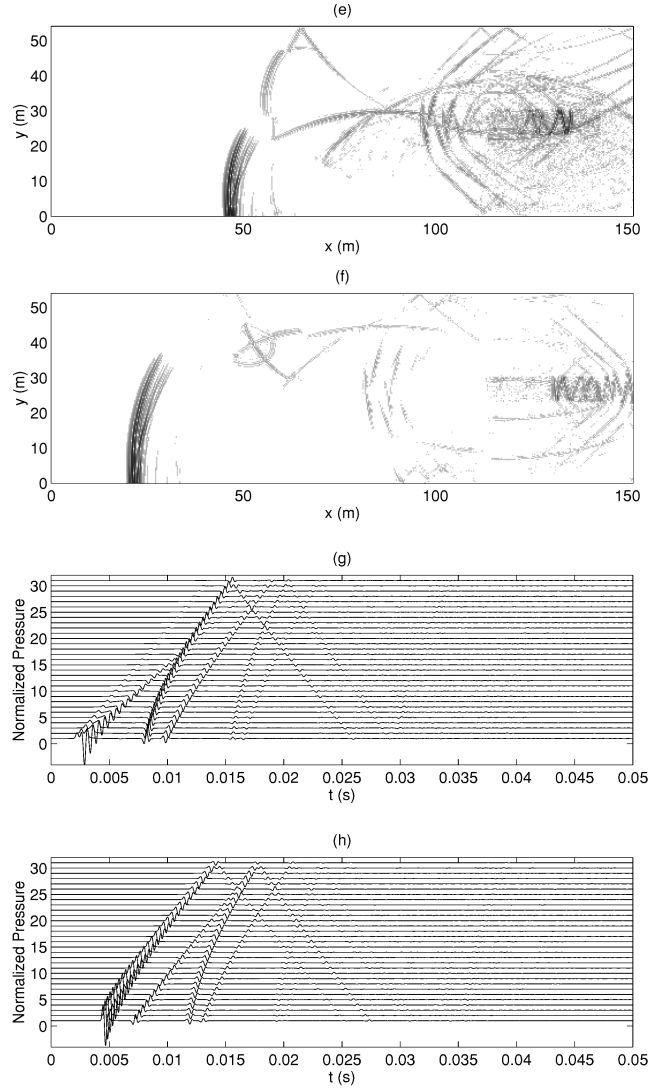


FIG. 12. 2-D simulation of a large problem in shallow water. (a) Geometry. From (b) to (f), snapshots of the absolute value of pressure field at time steps $n = 1000, 2000, 3000, 4000$, and 5000 , respectively (time-step size $\Delta t = 10 \mu s$). Pressure waveforms at the bottom (g) and top (h) receiver arrays.

geometry shown in Fig. 12(a) describes a problem with three layers (a top air layer, sea water, and the dipping sea floor). Acoustic wave propagation in such a medium with a wedge is a common problem important to many applications in shallow-water acoustics. In this example, the air–ocean interface is simulated as a soft boundary in order to reduce the number of unknowns in the problem. (The acoustic wavelength in the air is substantially shorter than in water and the sea floor. The full problem, including the wave propagation in the air, requires about 25 and 125 times more unknowns than using this treatment with soft boundary for 2-D and 3-D, respectively.) Therefore, the top air layer need not be included in the computational domain, even though it is shown in the figure. The sea water has parameters $\rho_1 = 1000 \text{ kg/m}^3$, $c_1 = 1500 \text{ m/s}$, $\gamma_1 = 10^{-4} \text{ s/m}^2$. The dipping sea floor has parameters $\rho_2 = 2200 \text{ kg/m}^3$, $c_2 = 2500 \text{ m/s}$, $\gamma_2 = 0 \text{ s/m}^2$. Within the seawater there are several objects (a large rectangular block of size $30 \times 7.5 \text{ m}^2$, seven small circular cylinders of radii 1.5 m , and a larger circular cylinder of radius 10 m) all with $\rho_3 = 2000 \text{ kg/m}^3$, $c_3 = 2000 \text{ m/s}$, $\gamma_3 = 0 \text{ s/m}^2$. A monopole line source is located right below



the rectangular block, while two arrays of receivers are mounted below and above the rectangular object, as shown in the figure.

At the highest frequency (5 kHz, or roughly 2.5 times the central frequency of the source time function), this large problem is of dimension $505.5\lambda \times 180.5\lambda$ in terms of the smallest wavelength in the water ($\lambda = 0.3$ m). The problem is discretized into 4044×1444 cells (or 23.36 million unknown scalar field variables) with $\Delta x = \Delta y = 0.0375$ m, and the time-step size is $\Delta t = 10 \mu\text{s}$.

The 2-D FDTD program is used to simulate the acoustic wave propagation in this medium. Figure 12(b)–(f) displays the snapshots at time steps $n = 1000, 2000, 3000, 4000$, and 5000, respectively. Note that in order to increase the contrast in the figures, we display the absolute value of pressure field. Very complex wave interactions with the medium are observed even at the early time. The source generates a wave inside the rectangular object which creates multiple reflections. Because of the faster sound speed inside this object than the ambient medium, these multiple reflections leak out energy continuously. The waves at the circular objects on the bottom surface form an interesting interference pattern. Shown in Fig. 12(g) and (h) are the pressure waveforms at the bottom and top receiver arrays. A striking difference between these two sets of waveforms is the presence of the head waves along the bottom surface of the rectangular object which are recorded at the bottom receiver array. From Fig. 12(g), it is observed that these head waves (i.e., the first arrivals) propagate with a speed of the sound speed of the rectangular object. The fast decaying direct wave is also present on the bottom receiver array.

It is again worthwhile to emphasize that, given the discontinuities intersecting the computational edge, other absorbing boundary conditions cannot be used to simulate this complex medium because of the numerical instability. With the PML absorbing boundary condition, the 2-D and 3-D FDTD programs remain stable even with a single precision. These computer programs for absorptive media can be used to answer many interesting questions regarding the wave propagation in complex media.

H. A note on computational performance

The FDTD programs were implemented on supercomputers with parallel processors (IBM SP2 and HP SPP-2000 Exemplar) as well as SUN Ultra 1 Station. Because of the intention for parallel computers, the programs were written to treat the PML and interior regions (see Fig. 1) in the same way, that is, the interior region is treated as a PML region with $e_\eta = 1$. In this way the boundary layers do not require a separate code. Of course, if the programs are intended for serial computers, then it will be more efficient to treat the interior region differently from the PML region so that the total memory requirement is slightly less. On an IBM SP2 single processor, the memory requirement for the above large 2-D problem (with 23.36 million unknowns) is about 390 Mbytes, and the CPU time is 6.17 s per time step. This is considered quite efficient given that only nominal optimization has been done on the programs. Further reduction in

the memory and CPU requirement is possible if the finite-difference coefficients are saved only for distinct regions.

IV. CONCLUSIONS

The perfectly matched layer (PML) absorbing boundary condition is applied to simulate acoustic waves in absorptive media. Within the boundary region of the computational domain, perfectly matched layers are used to attenuate outgoing acoustic waves. In contrast to elastic waves, the PML for scalar acoustic waves does not require a splitting in the velocity field components because the second-rank stress tensor collapses to a zero-rank tensor (i.e., a scalar) in the acoustic case. When there is an intrinsic attenuation, an additional term involving the time-integrated pressure field has to be introduced to account for the coupling between the loss from the PML and the normal absorption. This new absorbing boundary condition is stable even when a dipping interface intersects the computational edge, and is thus very useful in simulations of underwater acoustic waves. The PML absorbing boundary condition is implemented for two and three dimensions, and the computer programs have been validated by analytical solutions and other numerical results with Liao's absorbing boundary condition. This algorithm is ideal for parallel computation since the same code can be used for the inner computational domain and for the outer boundary. The extension to viscoelastic waves can be formulated similarly and is the subject of future studies.

ACKNOWLEDGMENTS

This work was supported by a Presidential Early Career Award for Scientists and Engineers (PECASE) through the Environmental Protection Agency and by Sandia National Laboratories under the SURP program.

- ¹C. Cerjan, D. Kosloff, R. Kosloff, and M. Reshef, "A nonreflecting boundary condition for discrete acoustic and elastic wave equations," *Geophysics* **50**, 705–708 (1985).
- ²A. R. Levander, "Use of the telegraphy equation to improve absorbing boundary efficiency for fourth-order acoustic wave finite difference schemes," *Bull. Seismol. Soc. Am.* **75**(6), 1847–1852 (1985).
- ³R. Clayton and B. Engquist, "Absorbing boundary conditions for acoustic and elastic wave equations," *Bull. Seismol. Soc. Am.* **67**, 1529–1540 (1977).
- ⁴E. L. Lindman, "Free-space boundary conditions for the time dependent wave equation," *J. Comput. Phys.* **18**, 66–78 (1975).
- ⁵C. J. Randall, "Absorbing boundary condition for the elastic wave equation: Velocity-stress formulation," *Geophysics* **54**, 1141–1152 (1989).
- ⁶Z. P. Liao, H. L. Wong, B. P. Yang, and Y. F. Yuan, "A transmitting boundary for transient wave analysis," *Sci. Sinica A* **27**, 1063–1076 (1984).
- ⁷R. L. Higdon, "Numerical absorbing boundary conditions for the wave equation," *Math. Comput.* **49**, 65–90 (1987).
- ⁸C. Peng and M. N. Toksöz, "An optimal absorbing boundary condition for finite difference modeling of acoustic and elastic wave propagation," *J. Acoust. Soc. Am.* **95**, 733–745 (1994).
- ⁹J.-P. Berenger, "A perfectly matched layer for the absorption of electromagnetic waves," *J. Comput. Phys.* **114**, 185–200 (1994).
- ¹⁰W. C. Chew and W. H. Weedon, "A 3D perfectly matched medium from modified Maxwell's equations with stretched coordinates," *Microw. Opt. Technol. Lett.* **7**, 599–604 (1994).
- ¹¹W. C. Chew and Q. H. Liu, "Perfectly matched layers for elastodynamics: A new absorbing boundary condition" Schlumberger–Doll Research Technical Report, August 1995.

- ¹²W. C. Chew and Q. H. Liu, "Using perfectly matched layers for elastodynamics," in *Proceedings of the IEEE Antennas Propagation Society International Symposium* (IEEE, New York, 1996), Vol. 1, pp. 366–369.
- ¹³W. C. Chew and Q. H. Liu, "Perfectly matched layers for elastodynamics: A new absorbing boundary condition," *J. Comput. Acoust.* **4**(4), 72–79 (1996).
- ¹⁴F. D. Hastings, J. B. Schneider, and S. L. Broschat, "Application of the perfectly matched layer (PML) absorbing boundary condition to elastic wave propagation," *J. Acoust. Soc. Am.* **100**, 3061–3069 (1996).
- ¹⁵Q. H. Liu, "An FDTD algorithm with perfectly matched layers for conductive media," *Microw. Opt. Technol. Lett.* **14**(2), 134–137 (1997).
- ¹⁶H. A. Kramers, *Atti Congr. Internaz. Fisici*, Como, Italy, Sept. 1927.
- ¹⁷Q. H. Liu and C. Chang, "Compressional head waves in attenuative formations: Forward modeling and inversion," *Geophysics* **61**(6), 1908–1920 (1996).
- ¹⁸Q. H. Liu, F. Daube, C. Randall, E. Schoen, H. Liu, and P. Lee, "A three-dimensional finite difference simulation of sonic logging," *J. Acoust. Soc. Am.* **100**, 72–79 (1996).